NUMERICAL INVESTIGATION OF SELF-SUSTAINED LIMIT-CYCLE OSCILLATIONS IN A FLAPPING-FOIL ENERGY HARVESTER

Enhao Wang[1], Kiran Ramesh[1], Ignazio Maria Viola[2], Shaun Killen[3]

[1]Aerospace Sciences Division,School of Engineering
University of Glasgow
Glasgow, UK, G12 8QQ
enhao.wang@glasgow.ac.uk
kiran.ramesh@glasgow.ac.uk

[2]Institute for Energy Systems, School of Engineering
University of Edinburgh
Edinburgh, UK, EH9 3DW
i.m.viola@ed.ac.uk

[3]Institute of Biodiversity, Animal Health, and Comparative Medicine
University of Glasgow
Glasgow, UK, G12 8QQ
shaun.killen@glasgow.ac.uk

Abstract:

Two-degree-of-freedom (2DOF) fully passive motion of a flapping foil at a low Reynolds number Re = 10,000 is studied numerically. The simulations are conducted using open source computational fluid dynamics (CFD) toolbox OpenFOAM. The present research is mainly focused on the self-sustained limit-cycle oscillations of a flapping foil with potential application as a hydro-energy harvester. The effect of different parameters on the onset of linear flutter, the characteristics of the system response, the available power from a flapping foil and the flow patterns are investigated. It is found that given a small initial perturbation, the response of the foil is similar to that of classical linear flutter i.e., the oscillations converged to a constant value at reduced velocities lower than the flutter velocity and limit-cycle oscillations (LCOs) are observed once the reduced velocities are greater than the flutter velocity. The reduced frequency of the LCOs exhibits a decreasing trend with increasing reduced velocity. In contrast, the phase difference between pitch and plunge increases with the increase of the reduced velocity. The feasibility of power extraction is demonstrated and the time-averaged power shows a single peak at an intermediate reduced velocity. Limit-cycle oscillations are found to be influenced by leading-edge vortex shedding as well as trailing-edge flow separation.

Keywords: energy harvesting, leading edge vortices, flapping wings, CFD, fluid structure interaction

1 INTRODUCTION

Ever-increasing energy demand coupled with the need to reduce greenhouse gas emissions has made innovative measures for energy generation necessary. Replacement of coal, oil and gas in

the generation of electric power can only be achieved by a mix of renewable strategies. Water (in the form of tides, oceanic currents and rivers) has the potential to provide up to three terawatts of power globally [1]. It is more predictable than wind and is an attractive option for countries with long coastlines. The majority of existing designs for water-based energy harvesting devices utilize horizontal-axis or vertical-axis turbines. These designs present several challenges related to economic viability as well as environmental impact [2]. Recently, novel energy harvesters mimicking the motion of fish tails have been developed, using the motion of a flapping wing to drive a generator [1]. The flapping-wing energy harvester offers promise of power generation at lower flow velocities, with no centrifugal stress associated with rotating blades, and with lesser noise generation and impact on the environment owing to lower tip speeds [1, 2]. In this concept, a constrained flapping wing, undergoes sustained oscillations when subject to adequate freestream flow velocity. Unlike conventional aerodynamic wings and rotary turbines which require smooth attached flow for maximum efficiency, these energy harvesters mimic fish swimming in nature by promoting the formation of large vortical structures. In particular, a leading-edge vortex is periodically formed and shed to achieve high instantaneous forces [3–6] and high propulsive [7] and power-extraction [8] efficiencies. The sustained oscillation of the flapping wing results from fluid dynamic flutter, at freestream velocities at and above the linear flutter velocity.

Early works on theory of flutter based on linear aerodynamic formulations by Theodorsen [9] and Theodorsen and Garrick [10] can predict the flutter velocity for the case of 2DOF wing. However, fluid dynamics nonlinearities may result from viscous effects [11] at low Reynolds numbers such as those considered in this study. Amandolese et al. [12] conducted wind tunnel tests to study the low speed flutter and limit-cycle oscillations of a 2DOF flat plate at Re $\sim$ 2.5×10^4. Their experimental results revealed the significant effect of nonlinear aerodynamics on the flutter boundary and the post-critical behavior. Ramesh et al. [13] investigated the effect of aerodynamic and structural parameters on the response of a 2DOF flat plate using a discrete-vortex method that allows for intermittent leading-edge vortex shedding through a leading-edge suction parameter (LESP). Their research showed that nonlinearity in the aerodynamics resulting from leading-edge vortex shedding is sufficient to result in limit-cycle behavior. At velocities just over the linear flutter velocity, single-period LCOs were seen, while at higher velocities, multi-period LCOs and subsequently divergent behavior were seen. It was also shows that the addition of positive cubic stiffening to the system, a structural nonlinearity, resulted in a larger velocity range of single-period LCOs (albeit of smaller amplitudes) and increased the velocity at which divergent behavior occurs.

High-fidelity CFD methods have also been used to model 2DOF fully passive flapping of a foil. Peng and Zhu [14] used a Navier-Stokes model to study energy harvesting through flow-induced oscillations of a fully passive foil. They found that the interaction between the leading-edge vortex and the foil can enhance the energy harvesting performance in fully passive motions. Moreover, they suggest that the pivot location is an important factor to the energy harvesting capacity. Young et al. [15] used commercial CFD package ANSYS FLUENT 14.0 [16] to study the power generation from a fully passive flapping foil. The authors reported that the key to improving the efficiency of energy extraction from the flow is to control the timing of the formation and location of the leading-edge vortex at crucial times during the flapping cycle and the interaction of the vortex with the trailing edge. A a more recent numerical study by Wang et al. [17] suggested that high-efficiency case in fully passive flapping motions is associated with a large pitch-plunge phase and a "2S" wake pattern composed of two strong single leading-edge vortices shed per cycle.

2

In this paper, the open source computational fluid dynamics (CFD) toolbox OpenFOAM [18] is coupled with a 2DOF structural model to study the fluid-structure interaction and limit-cycle oscillations of a flat plate at a low Reynolds number Re = 10,000. The outline of the rest of the paper is as follows. A detailed introduction to the numerical methods is provided in Section 2. In Section 3, the problem descriptions are summarized. The numerical results and presented and analyzed in Section 4 and this paper concludes in Section 5.

2 NUMERICAL METHODS

A sketch of the physical configuration of the aeroelastic system is shown in Figure 1(a). The fluid flow around the flat plate is modeled by solving the unsteady incompressible Navier-Stokes equations in conjunction with the Spalart-Allmaras turbulence model [19]. The basic governing equations are as follows.

$$\frac{\partial u_i}{\partial x_i} = 0 \tag{1}$$

$$\frac{\partial u_i}{\partial t} + u_j \frac{\partial u_i}{\partial x_j} = -\frac{1}{\rho}\frac{\partial p}{\partial x_i} + \frac{\partial}{\partial x_j}(2\nu S_{ij} - \overline{u'_j u'_i}) \tag{2}$$

where u_i is the velocity component in the x_i direction, t is the time, ρ is the fluid density, p is the pressure, ν is the kinematic viscosity of the fluid, and S_{ij} is the rate of strain tensor.

$$S_{ij} = \frac{1}{2}(\frac{\partial u_i}{\partial x_j} + \frac{\partial u_j}{\partial x_i}) \tag{3}$$

The quantity $\tau_{ij} = -\overline{u'_j u'_i}$ is the Reynolds stress tensor. In the Spalart-Allmaras model, the Boussinesq approximation is employed to related the Reynolds stress tensor to the rate of strain tensor.

$$\tau_{ij} = 2\nu_T S_{ij} \tag{4}$$

where ν_T is the turbulent eddy viscosity and the related defining equations are $\nu_T = \widetilde{\nu} f_{v1}$, $f_{v1} = \chi^3/\chi^3 + c_{v1}^3$, $\chi = \widetilde{\nu}/\nu$, $\widetilde{\nu}$ is an intermediate working variable of the turbulence model and obeys the following transport equation.

$$\frac{\partial \widetilde{\nu}}{\partial t} + u_j \frac{\partial \widetilde{\nu}}{\partial x_j} = c_{b1}\widetilde{S}\widetilde{\nu} - c_{w1}f_w(\frac{\widetilde{\nu}}{d})^2 + \frac{1}{\sigma}\{\frac{\partial}{\partial x_j}[(\nu + \widetilde{\nu})\frac{\partial \widetilde{\nu}}{\partial x_j}] + c_{b2}\frac{\partial \widetilde{\nu}}{\partial x_i}\frac{\partial \widetilde{\nu}}{\partial x_i}\} \tag{5}$$

where c_{b1}, c_{w1}, c_{b2} and c_{v1} are model coefficients and the values are $c_{b1} = 0.1355$, $c_{w1} = \frac{c_{b1}}{\kappa^2} + \frac{1+c_{b2}}{\sigma}$, $c_{b2} = 0.622$, $c_{v1} = 7.1$, where $\kappa = 0.41$ and $\sigma = 2/3$. In this study, the trip terms f_{t1} and f_{t2} in the originally published version are turned off and at the same time the 'Trip-less' initial condition for $\widetilde{\nu}$ is used following Travin et al. [20].

The governing equations are solved using the open source CFD toolbox OpenFOAM based on a finite volume method (FVM). A second-order backward implicit scheme is adopted to discretise the transient terms, while second-order Gaussian integration schemes with linear interpolation for the face-centered values of the variables are used for the gradient, divergence and Laplacian terms. The pressure implicit with splitting of operators (PISO) algorithm is employed to achieve pressure-velocity coupling.

A close-up of the computational mesh is presented in Figure 1(b). There are 560 nodes along the circumference of the flat plate and the minimum mesh size next to the flat plate surface in the radial direction is $0.001c$, where c is the chord length of the flat plate. The non-dimensional mesh size next to the flat plate surface is found to be $y^+ < 1$, where y^+ is defined as $y^+ = u_f y/\nu$ with u_f being the friction velocity and y being the distance to the nearest wall. The boundary conditions for the governing equations are as follows. The surface of the flat plate is assumed to be smooth, where no-slip boundary condition is employed. The inflow velocity and turbulence properties are set to be the same as the freestream values. At the outflow boundary, the gradients of the flow velocity in the streamwise direction is set to zero and the same turbulence properties as the freestream ones are considered. On the two transverse boundaries, the velocity in the direction normal to the boundary is zero and the freestream turbulence properties are adopted. As for the pressure boundary conditions, zero normal gradient of the pressure is applied to all the boundaries expect the outflow boundary where the pressure is given a reference value of zero.
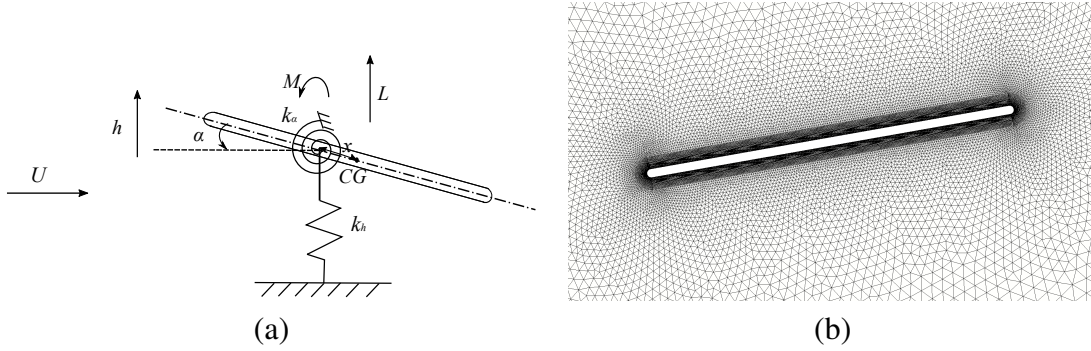

| (a) | (b) |

Figure 1: (a) Sketch of the physical configuration and (b) computational mesh.

The plunging and pitching motions of the flat plate can be described by the second-order oscillators:

$$m\ddot{h} - S_\alpha \cos\alpha + S_\alpha \dot{\alpha}^2 \sin\alpha + k_h h = L \qquad (6)$$

$$-S_\alpha \cos\alpha + I_\alpha \ddot{\alpha} + k_\alpha \alpha = M \qquad (7)$$

where m is the mass of the flat plate, h is the plunge displacement, $k_h = m\omega_h^2$ is the plunge stiffness, ω_h is the characteristic frequency of plunge mode, I_α is the moment of inertia about the elastic axis, α is the pitch angle, $k_\alpha = I_\alpha \omega_\alpha^2$ is the pitch stiffness and ω_α is the characteristic frequency of the pitch mode. S_α is the static moment of the flat-plate model about the elastic axis. L and M are the lift and pitching moment about the elastic axis, respectively. Eqs. (6) and (7) are solved using a Newmark integration method [21] with $\alpha(0) = 10°$ and $\dot{\alpha}(0) = h(0) = \dot{h}(0) = 0$.

The fluid-structure interaction is based on a loosely coupled approach in which information is exchanged at each time step, but no subiterations are included. Within each time step, the flow equations are solved to obtain the forces and moments on the flat plate. The forces and moments are then applied to the structural dynamic equations to yield the motion quantities of the flat plate. After that, spherical linear interpolation (SLERP) of the motion quantities as a function of distance to the objective surfaces is performed to update the computational mesh and the next time step begins with solving the flow equations on the updated mesh.

3 PROBLEM DESCRIPTION

The structural and aerodynamic parameters of the 2DOF flat plate are defined in this section. The Reynolds number based on the freestream velocity $U = 0.1312$ m/s and the chord length c = 0.0762 m of the flat plate is $Re = Uc/\nu = 10,000$. The base parameter set for the present simulations are summarized in Table 1. A 2.3%-thick flat plate with semi-circular leading and trailing edges is considered. The chord length is chosen as a reference length scale. The non-dimensional distance of the pivot aft of the leading edge is $x_p = 0.35$, the non-dimensional static unbalance of the flat plate is $x_\alpha = 0.05$, the non-dimensional radius of gyration of the flat plate about its pivot is $r_\alpha = 2\sqrt{I_\alpha/mc^2} = 0.5$, the inverse mass ratio is $\kappa = \pi\rho c^2/4m$, where m is mass per unit span of the flat plate and different frequency ratios $\overline{\omega} = \omega_h/\omega_\alpha$ are considered.

Table 1: Base parameter set used in the present study.

Parameter	Symbol	Value
Distance of pivot aft of leading edge	x_p	$0.35c$
Static unbalance	x_α	$0.05c$
Radius of gyration	r_α	0.5
Inverse mass ratio	κ	0.05

The mesh dependency study is conducted by simulating the fully passive flapping of a flat plate with a frequency ratio $\overline{\omega} = 0.25$ at a reduced velocity $U^* = U/\omega_\alpha c = 1.6$. The properties of the three meshes are listed in Table 1, where N_{node}, N_c, Δr are the total number of nodes, the node number along the circumference of the flat plate and the minimum mesh size near the flat plate surface in the radial direction, respectively.

Table 2: Comparison of results from the three meshes.

Mesh	N_{node}	N_c	$\Delta r/c$	h/c	α (deg)	k
1	24488	560	0.005	0.2429	64.1864	0.3341
2	48590	1120	0.001	0.2405	65.8029	0.3341
3	99576	2240	0.0005	0.2402	65.9132	0.3341

It can be seen from Table 2 that the reduced frequency k computed from the three meshes are identical. The maximum difference between Mesh 1 and Mesh 2 is 2.46% which is observed in pitch angle α, while it reduces to only 0.17% between Mesh 2 and Mesh 3. In the consideration of both accuracy and computational efforts, Mesh 2 is used in the CFD simulations of the present study.

4 RESULTS AND DISCUSSIONS

Numerical simulations are performed to investigate the response of a 2DOF fully passive foil subject to uniform flow at a low Reynolds number Re = 10,000.

4.1 Bifurcation Behavior of Pitch and Plunge Response

Figure 2 shows the bifurcation characteristics of α and h/c as a function of the reduced velocity U^* for different frequency ratios. It can be seen that for all the frequency ratios considered in
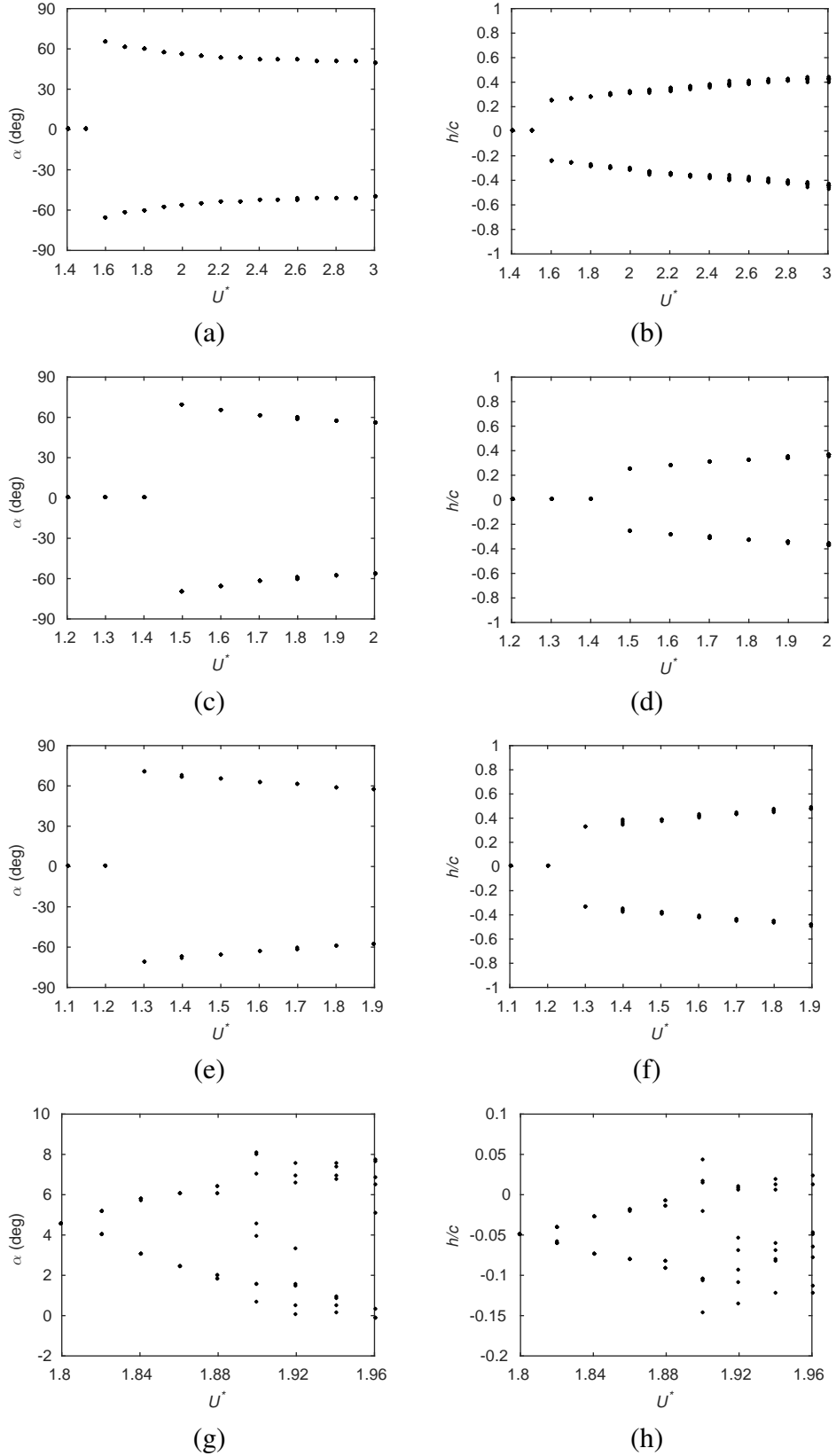
Figure 2: Bifurcation characteristics of α and h/c as a function of the reduced velocity U^* (values are taken at $d\alpha/dt = 0$ and $dh/dt = 0$): (a) α for $\overline{\omega} = 0.25$, (b) h/c for $\overline{\omega} = 0.25$, (c) α for $\overline{\omega} = 0.5$, (d) h/c for $\overline{\omega} = 0.5$, (e) α for $\overline{\omega} = 0.75$, (f) h/c for $\overline{\omega} = 0.75$, (g) α for $\overline{\omega} = 1$ and (h) h/c for $\overline{\omega} = 1$.

the present study, the oscillatory behavior of the flat plate is convergent at small U^*. Flutter occurs when U^* reaches the flutter velocity U_F^*. For $\overline{\omega} = 0.25 - 0.75$, the flutter response is single-period constant-amplitude limit-cycle oscillation. α decreases and h/c increases with the increase of U^*. In contrast, α and h/c both increase with U^* when $\overline{\omega} = 1$. Other evident difference in the response of the flat plate between $\overline{\omega} = 1$ and the other three frequency ratios considered in the present study are that there exist offsets in α and h/c and multi-amplitude oscillation is observed when U^* is high. As previous results for $\overline{\omega} = 1$ were quite limited, the present results for $\overline{\omega} = 1$ need to be further investigated.
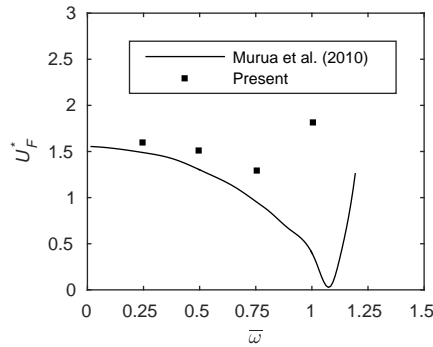
Figure 3: Flutter-onset velocities compared with data by Murua et al. (2010).

Figure 3 shows the comparison of the flutter-onset velocities at different frequencies ratios between the present results and the data published by Murua et al. [22]. As shown in the figure, the decreasing trend of U_F^* with the increase of $\overline{\omega}$ for $\overline{\omega} = 0.25 - 0.75$ in the present results agrees with that of Murua et al. with the values U_F^* in the present study being higher than those by Murua et al. As $\overline{\omega}$ increases to 1, the results of Murua et al. exhibit a further decrease in U_F^*, whereas U_F^* in the present study increases to around 1.82. The discrepancies between the present results and the results of Murua et al. can be attributed to the viscous effects which is taken into account in the present CFD simulation but neglected in [22].

4.2 Detailed Study of Limit-Cycle Behavior

Figures 4 and 5 demonstrate the response of the flat plate for $\overline{\omega} = 0.25$ at $U^* = 1.6$ and 3, respectively. It is apparent that the limit-cycle oscillations of the flat plate at these two reduced velocities are single period. The single-period response is further affirmed by the PSD plots in Figures 4(g) and 5(g). Higher harmonic components are observed in the force and moment coefficients. According the Gsell et al. [23], these higher harmonics impact the transfer of energy between the flow and the moving body. A nearly circular shape phase-plane plot is observed for $U^* = 1.6$ reflecting that $d\alpha/dt^*$ is almost sinusoidal. The shape of the phase-plane plot changes when U^* increases to 3. The shape of the phase plane plot in Figure 5(f) indicates that $d\alpha/dt^*$ is no longer sinusoidal at $U^* = 3$.

The response of the flat plate for $\overline{\omega} = 1$ at $U^* = 1.84$ and 1.92 is presented in Figures 6 and 7. It can be seen from Figure 7 that the response of the flat plate shows single-period limit-cycle oscillation as well. However, the higher harmonic components in the force and moment coefficients disappear. Moreover, the phase-plane plot are not as coincident as those for $\overline{\omega} = 0.25$ indicating the modulations in $d\alpha/dt^*$. As for $U^* = 1.92$, the response of the flat plate is multi-amplitude. Several frequencies are observed in the PSD plot and the phase-plane plot is irregular.
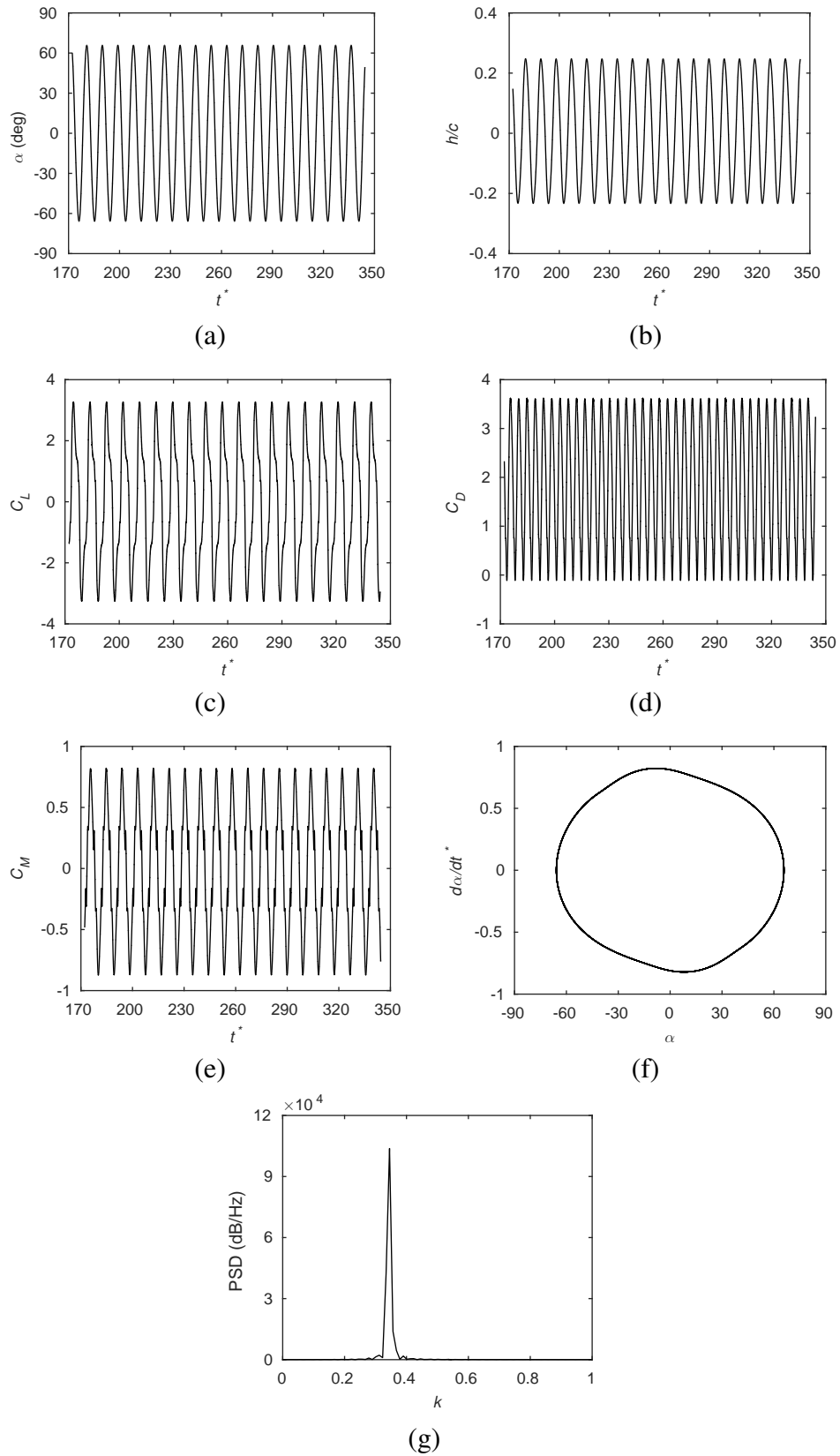
Figure 4: Response for $U^* = 1.6$ and $\overline{\omega} = 0.25$: (a) α, (b) h/c, (c) C_L, (d) C_D, (e) C_M, (f) phase-plane plot and (g) PSD plot.
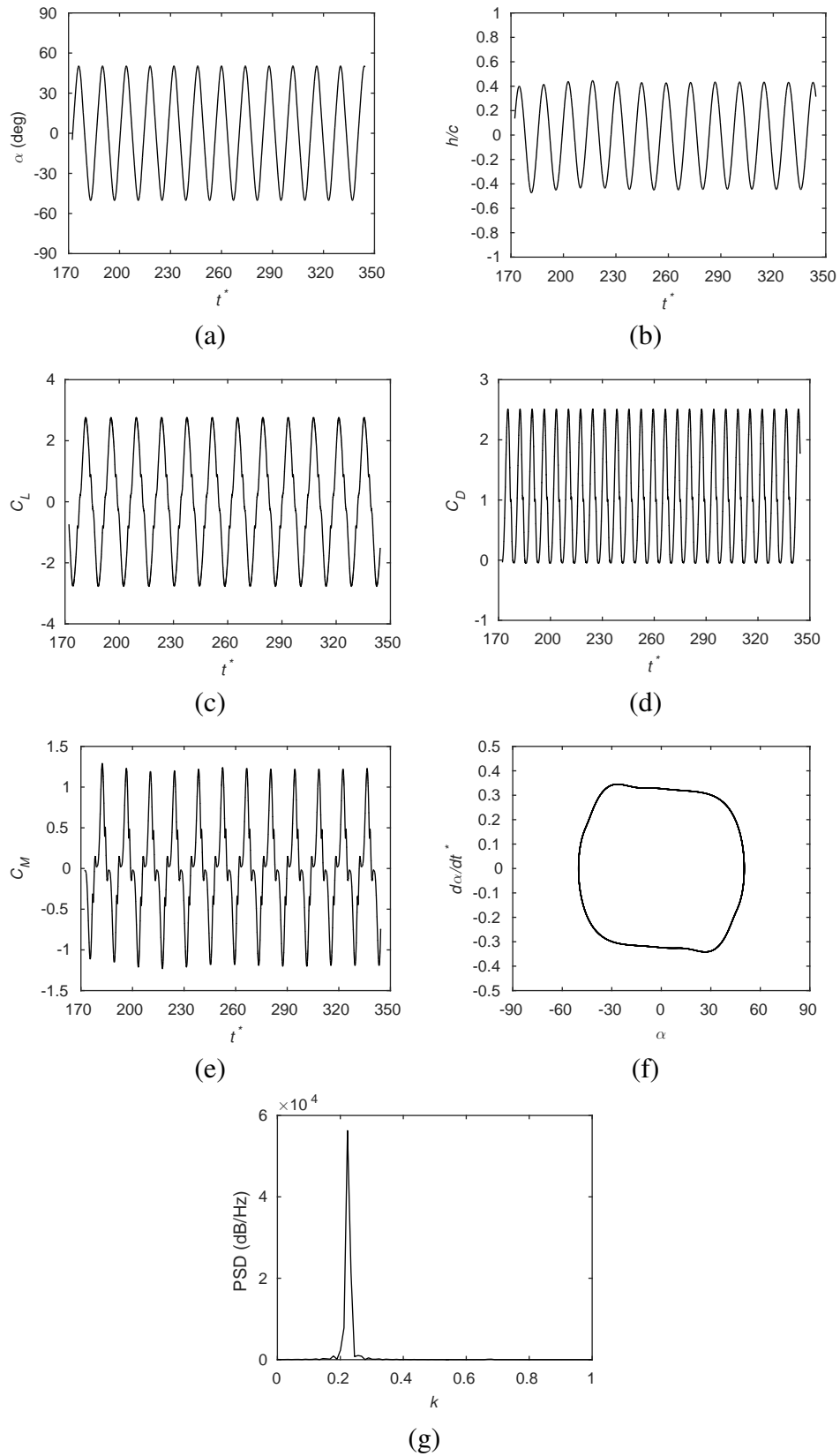
Figure 5: Response for $U^* = 3$ and $\overline{\omega} = 0.25$: (a) α, (b) h/c, (c) C_L, (d) C_D, (e) C_M, (f) phase-plane plot and (g) PSD plot.
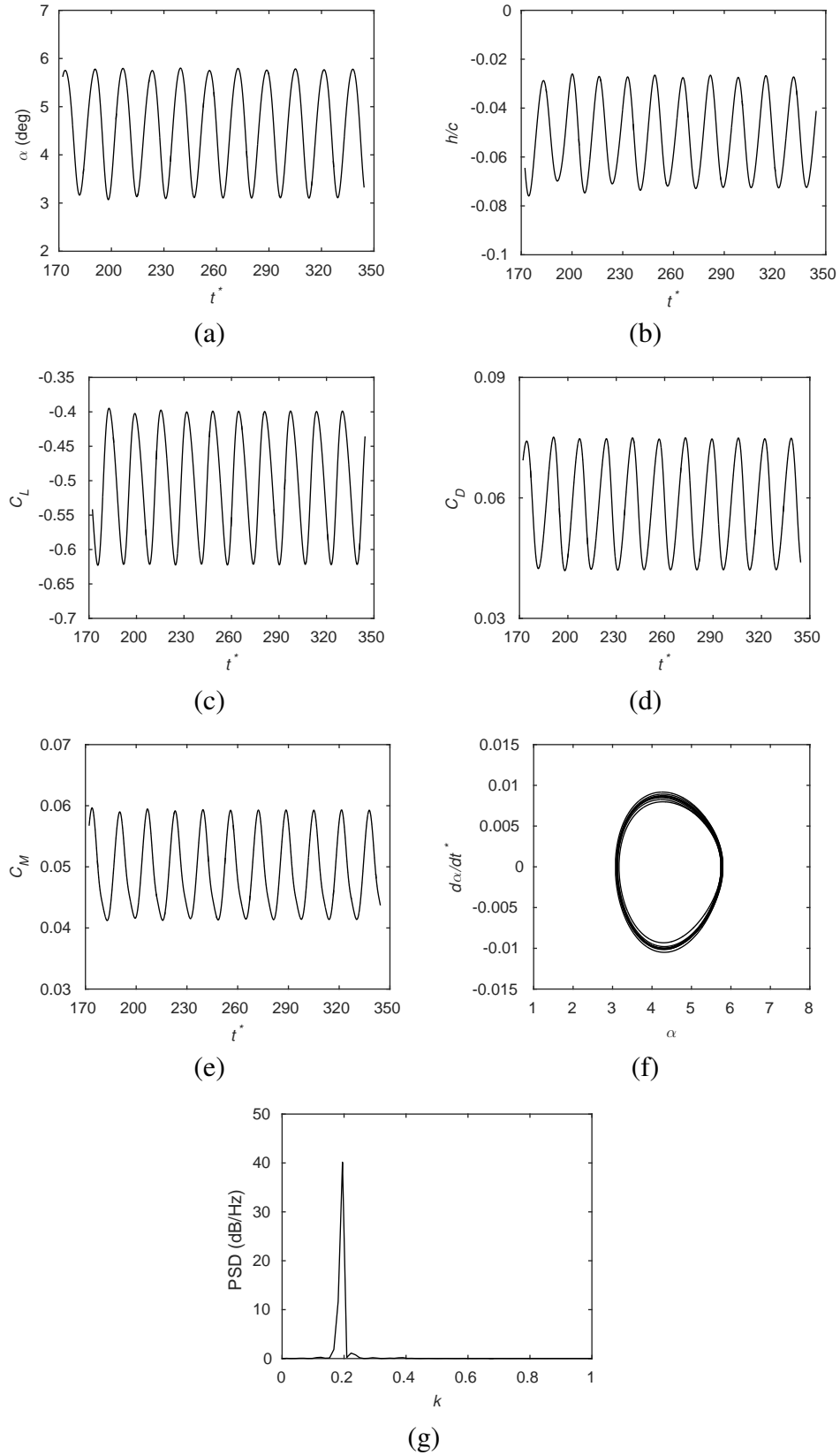
Figure 6: Response for $U^* = 1.84$ and $\overline{\omega} = 1$: (a) α, (b) h/c, (c) C_L, (d) C_D, (e) C_M, (f) phase-plane plot and (g) PSD plot.
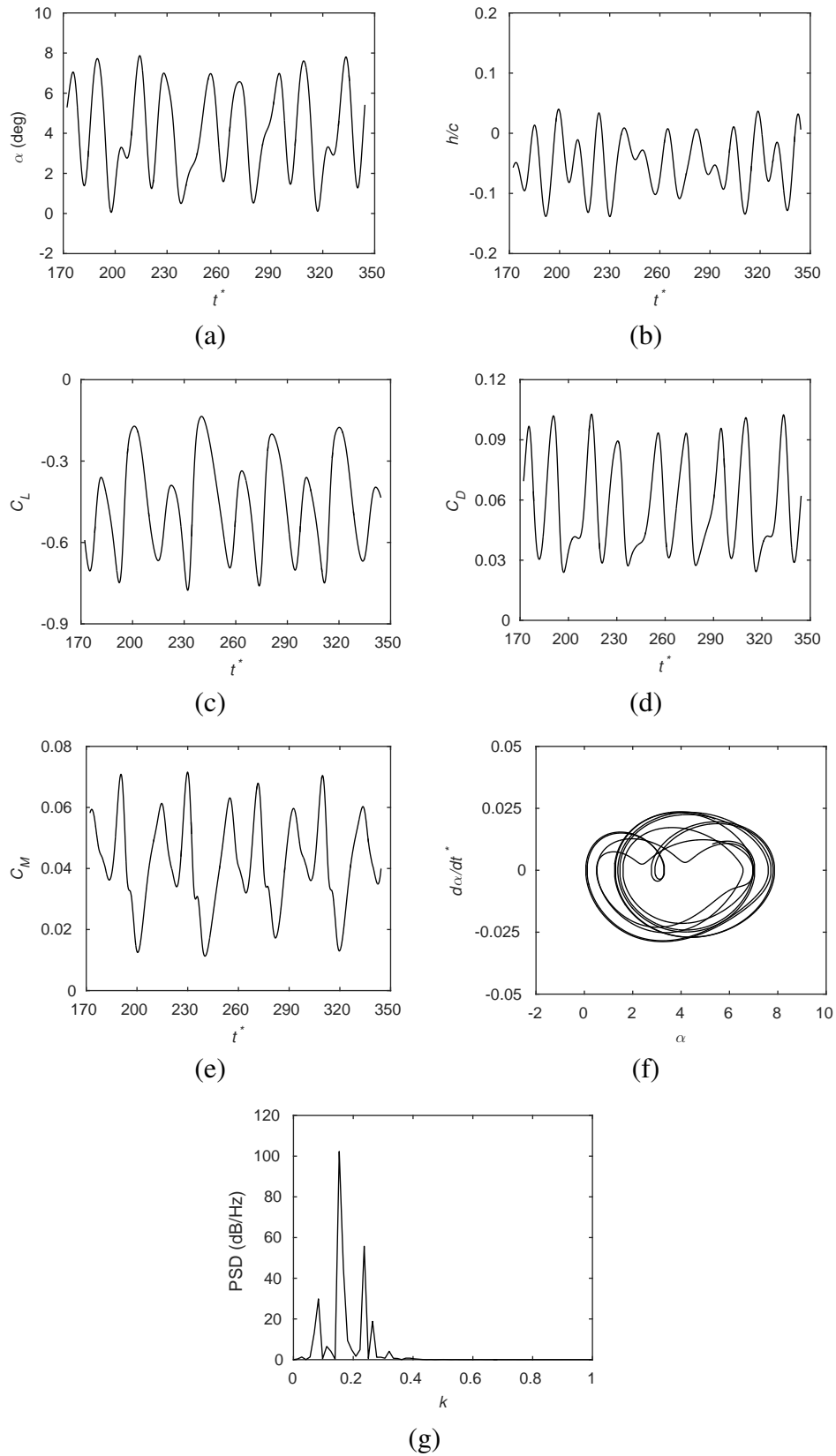
Figure 7: Response for $U^* = 1.92$ and $\overline{\omega} = 1$: (a) α, (b) h/c, (c) C_L, (d) C_D, (e) C_M, (f) phase-plane plot and (g) PSD plot.
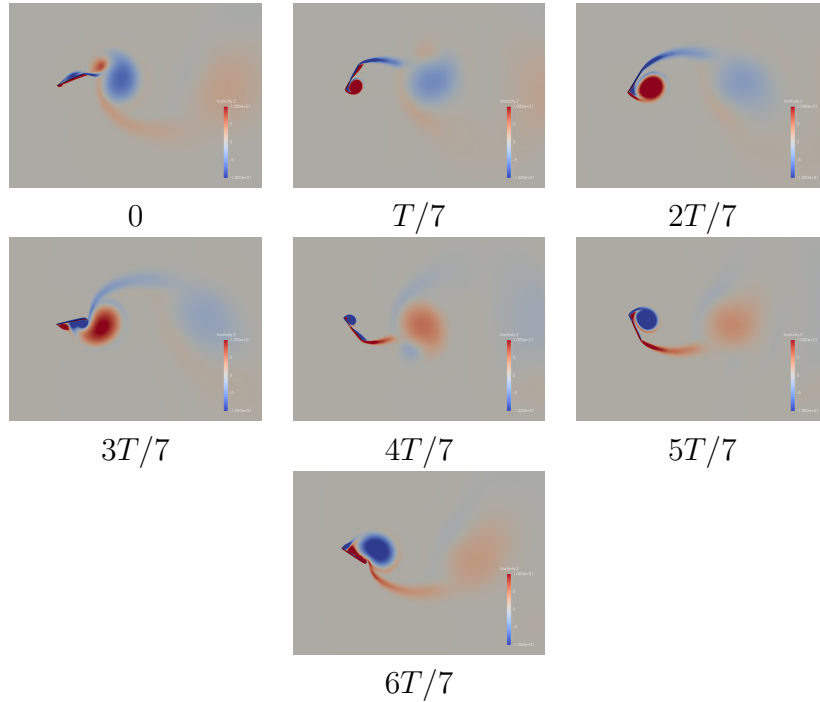
Figure 8: Spanwise vorticity ω_z contours at different time instants in one cycle for $U^* = 1.6$ and $\overline{\omega} = 0.25$.

We examined the flow around the flat plate when it is undergoing limit-cycle oscillations by plotting the spanwise vorticity (ω_z) contours. Figure 8 exhibits ω_z contours at different time instants in one cycle for $U^* = 1.6$ and $\overline{\omega} = 0.25$. It is observed that the flow is characterized by leading-edge vortex shedding, which agrees with the conclusions by Zhu [24] and Ramesh et al. [13]. In fact the leading-edge vortices play a key role in preventing the oscillations from diverging.

4.3 Effect of Initial Condition

A study on the effect of the initial conditions has also be conducted. Two initial conditions are considered (i.e., $\alpha_0 = 10°$ and $\dot{\alpha}_0 = 60°/s$) and CFD simulations are carried out for $U^* = 1.5$ and $\overline{\omega} = 0.25$. The comparison of the responses under the two initial conditions are given in Figure 9. It can be seen that the oscillations converge to zero when a small initial perturbation $\alpha_0 = 10°$ is given. In contrast, the response of the flat plate develops into limit-cycle oscillations if it is subject to a larger initial perturbation of $\dot{\alpha}_0 = 60°/s$. This is in accordance with the subcritical limit-cycle oscillations reported by Sarkar and Bijl [25] at low reduced frequencies, likely resulting from the aerodynamic nonlinearity of trailing-edge flow separation.

4.4 Summary of limit-cycle characteristics

A summary of the limit-cycle characteristics for $\overline{\omega} = 0.25$ - 0.75 is shown in Figure 10. It can be seen from Figures 10(a) and (b) that limit-cycle oscillations of the flat plate occur at reduced velocities at and above the flutter velocity (i.e., $U^* \geq U_F^*$). The oscillation amplitude increases slightly with the increase of $\overline{\omega}$. Figures 10(c) and (d) demonstrates the variation of the reduced frequency k and the phase difference between pitch and plunge ϕ with U^*/U_F^* for different frequency ratios. For all the three frequency ratios, k decreases with the increase of U^*/U_F^* while ϕ increases with the increasing U^*/U_F^*. Moreover, higher $\overline{\omega}$ results in higher k and larger ϕ.
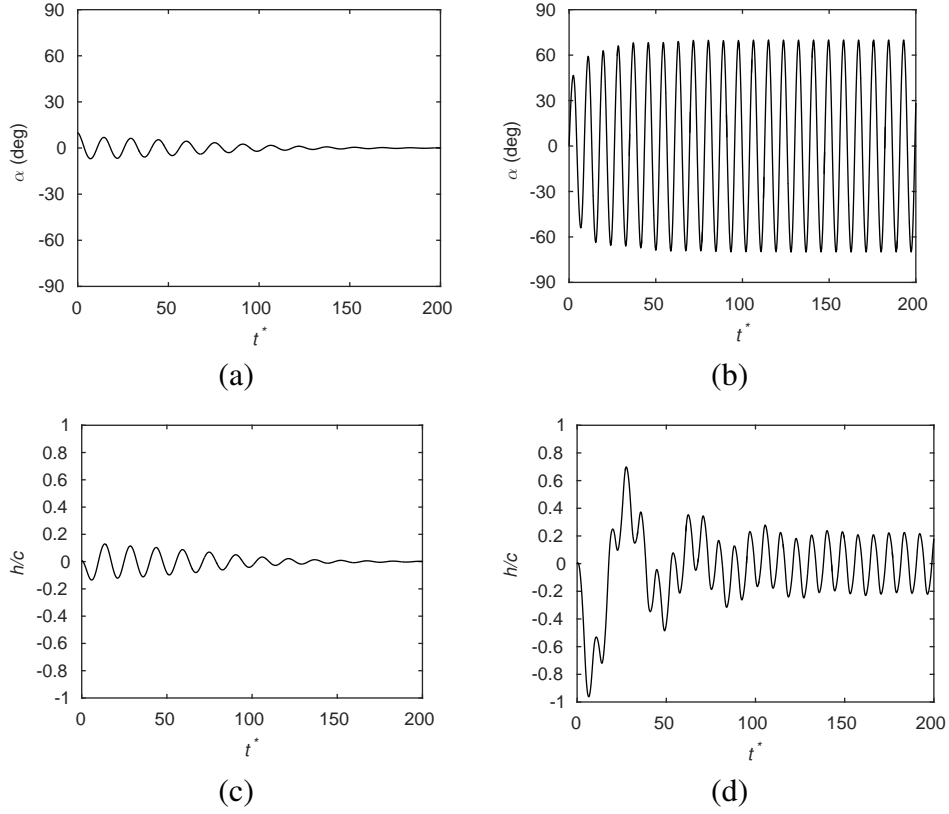
Figure 9: Effect of initial conditions on the response at $U^* = 1.5$ and $\overline{\omega} = 0.25$: (a) α for $\alpha_0 = 0°$, (b) α for $\dot{\alpha}_0 = 60°/s$,(c) h/c for $\alpha_0 = 0°$ and (d) h/c for $\dot{\alpha}_0 = 60°/s$.
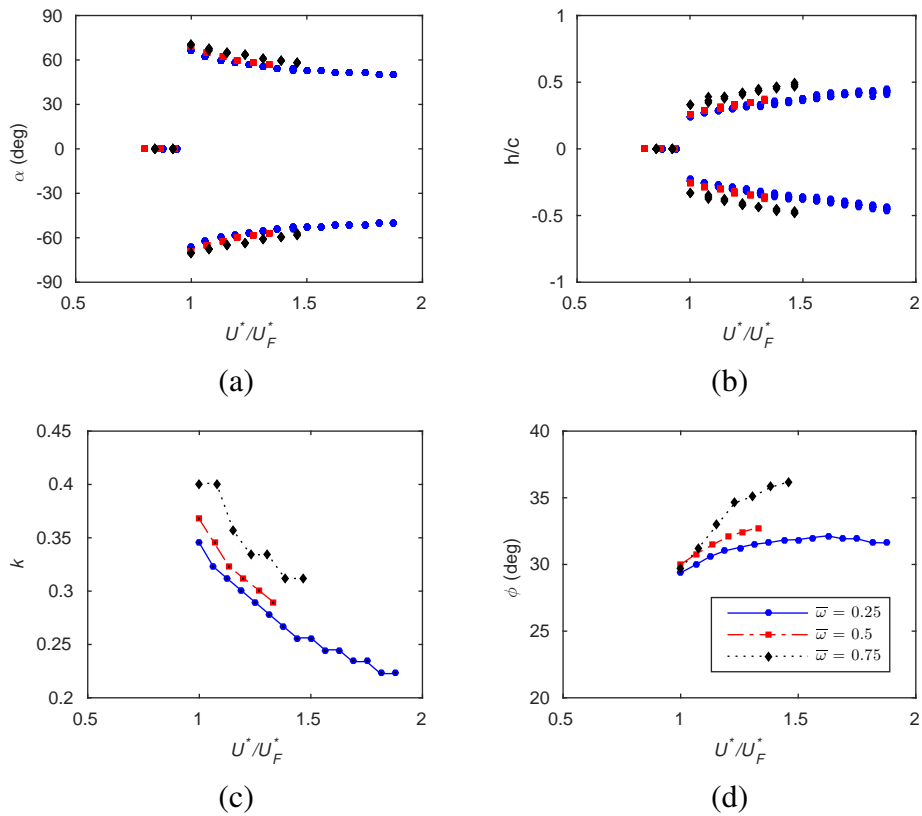
Figure 10: Summary of limit-cycle characteristics for $\overline{\omega}$ = 0.25 - 0.75: (a) α, (b) h/c, (c) k, (d) ϕ.

4.5 Analysis of Available Power

(a)

(b)
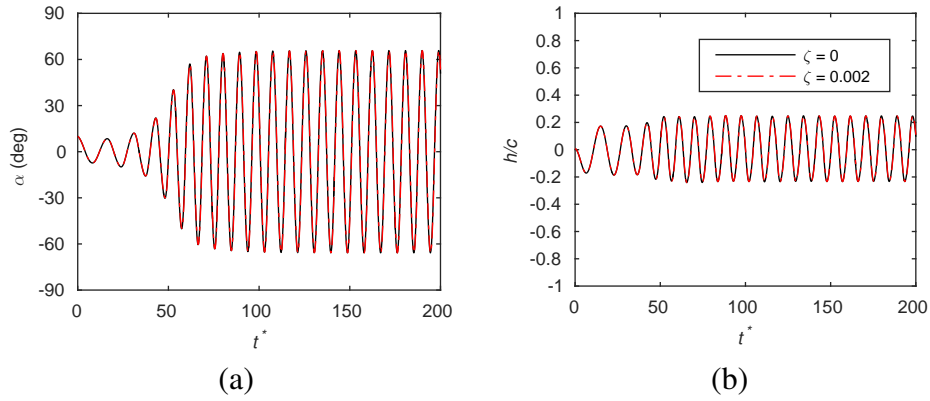
Figure 11: Comparison of responses of the flat plate with or without damping at $U^* = 1.6$ and $\overline{\omega} = 0.25$: (a) α and (b) h/c.
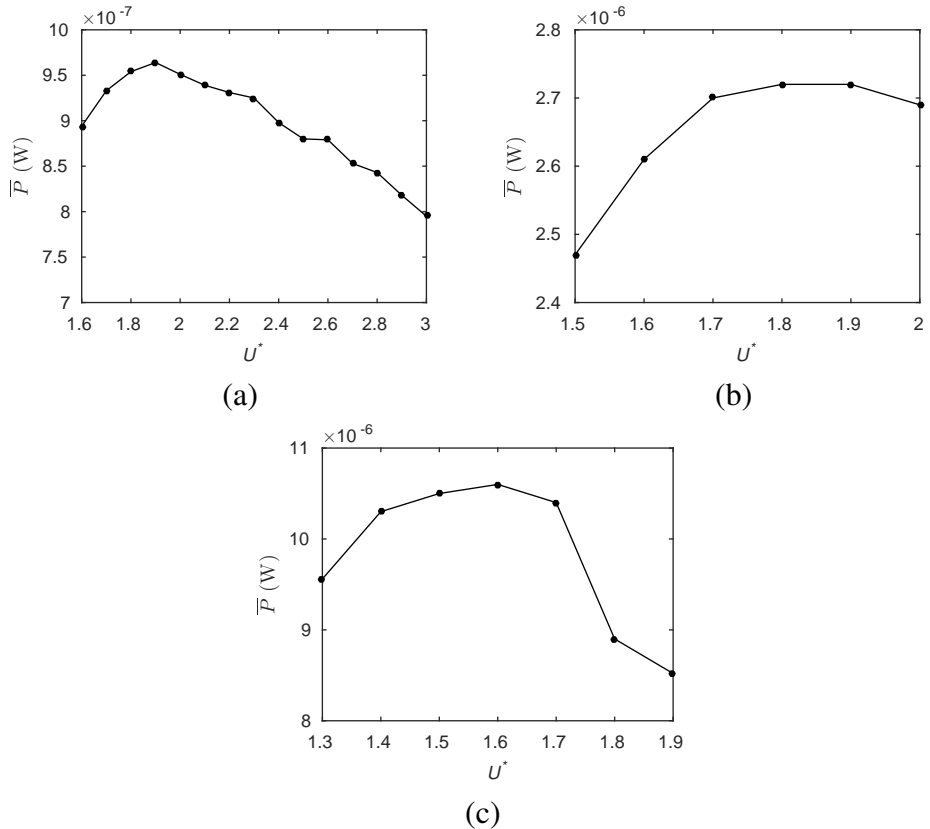

(a)

(b)

(c)

Figure 12: Variation of time-average power $\overline{P}$ with U^*: (a) $\overline{\omega} = 0.25$, (b) $\overline{\omega} = 0.5$ and (c) $\overline{\omega} = 0.75$.

The ideal regime for harvesting power from the 2DOF aeroelastic system is in the supercritical, single-period LCOs that occur above the flutter velocity. The time-averaged power from the flapping motion is examined. According to Xiao and Zhu (2014) [2], for self-sustained systems, if the motions are periodic, the time-averaged power from the plunging motion $\overline{P}$ can be calculated from the following equation.

$$\overline{P} = \frac{1}{T} \int_t^{t+T} c_0 \dot{h}^2 dt \tag{8}$$

14

where c_0 is the plunge damping coefficient. Although we neglected damping in the parametric study, we still want to illustrate the variation trend of $\overline{P}$ with U^*. Therefore, we considered a very low damping ratio $\zeta = 0.002$ to calculate the time-averaged power in each case so that the system dynamics are not changed.

Figure 11 shows the comparison of the response of the flat plate for $\zeta = 0$ and $\zeta = 0.002$. As shown in the figure, the effect of such a low damping on the response of the flat plate is almost negligible. Therefore, $\zeta = 0.002$ and the $\dot{h}$ for $\zeta = 0$ are used to estimate the available time-averaged power. Figure 12 shows the time-averaged power extractable from the plunging motion for $\overline{\omega} = 0.25 - 0.75$. For all the three frequency ratios, $\overline{P}$ first increases with increasing U^* then it decreases with the increase of U^* after it reaches its peak value. We noted that the present Re = 10,000 corresponds to a small wing of chord length of 0.0762 m in water flowing at 0.1312 m/s. This and the low value of damping employed (for illustration purposes) result in the small values of power observed. In actual implementation, such devices must be used in a large arrays for a good output.

5 CONCLUSIONS

Numerical simulations are performed to investigate limit-cycle oscillations of a 2DOF fully passive flat plate at Re = 10,000. The effect of different parameters on the onset of linear flutter, the characteristics of the system response and the flow patterns are investigated.

For all the frequency ratios considered, the response of the flat plate converge to a constant value if the reduced velocity is lower than the flutter velocity. Subcritical limit-cycle oscillations may also occur if a large initial perturbation is applied. At reduced velocity immediately greater than the flutter velocity, the flat plate's motion exhibits single-period limit-cycle behavior. The response of the flat plate for the high $\overline{\omega} = 1$ was an outlier.

The reduced frequency of the post-flutter LCOs decreases with the increase of the reduced velocity whereas the phase difference between pitch and plunge increases as the reduced velocity is increased.

The time-averaged power increases with the reduced velocity when the reduced velocity is low. After it reaches its peak value at an intermediate reduced velocity which designs of energy harvesters may take advantage of, it starts to decrease with the increasing reduced velocity.

Leading-edge vortex shedding and trailing-edge flow separation are found to be associated with the limit-cycle oscillations. Overall, the present CFD results showed general agreement with previous studies. Significant data has been generated which provides a proof-of-concept for the flapping-foil generator, and also informs design for maximizing output and efficiency. Our future research includes the effects of structural nonlinearities and the freestream flow conditions on the performance of flapping-wing energy harvester.

6 ACKNOWLEDGMENTS

7 REFERENCES

[1] Young, J., Lai, J., and Platzer, M. (2014). A review of the progress and challenges in flapping foil power generation. *Progress in Aerospace Sciences*, 67, 2 – 28.

[2] Xiao, Q. and Zhu, Q. (2014). A review on flow energy harvesters based on flapping foils. *Journal of Fluids and Structures*, 46, 174 – 191.

[3] Ellington, C., vanden Berg, C., Willmott, A., et al. (1996). Leading edge vortices in insect flight. *Nature*, 384, 626 – 630.

[4] Shyy, W. and Liu, H. (2007). Leading edge vortices in insect flight: The role of leading-edge vortices. *AIAA Journal*, 45, 2817 – 2819.

[5] Ellington, C. (1999). The novel aerodynamics of inset flight: applications to micro-air vehicles. *Journal of Experimental Biology*, 202, 3439 – 3448.

[6] Dickinson, M. and Gotz, K. (1993). Unsteady aerodynamic performance of model wings at low reynolds numbers. *Journal of Experimental Biology*, 174, 45 – 64.

[7] Anderson, J., Streitlien, K., Barrett, D., et al. (1998). Oscillating foils of high propulsive efficiency. *Journal of Fluid Mechanics*, 360, 41 – 72.

[8] Kinsey, T. and Dumas, G. (2008). Parametric study of an oscillating airfoil in a power-extraction regime. *AIAA Journal*, 46, 1318 – 1330.

[9] Theodorsen, T. (1935). General theory of aerodynamic instability and the mechanism of flutter. Tech. Rep. 496, NACA.

[10] Theodorsen, T. and Garrick, I. (1935). Flutter calculations in three degrees of freedom. Tech. Rep. 496, NACA.

[11] Lee, B., Price, S., and Wong, Y. (1999). Nonlinear aeroelastic analysis of airfoils: bifurcation and chaos. *Progress in Aerospace Sciences*, 35, 205 – 344.

[12] Amandolese, X., Michelin, S., and Choquel, M. (2013). Low speed flutter and limit cycle oscillations of two-degree-of-freedom flat plate in a wind tunnel. *Journal of Fluids and Structures*, 43, 244 – 255.

[13] Ramesh, K., Murua, J., and Gopalarathnam, A. (2015). Limit-cycle oscillations in unsteady flows dominated by intermittent leading-edge vortex shedding. *Journal of Fluids and Structures*, 55, 84 – 105.

[14] Peng, Z. and Zhu, Q. (2009). Energy harvesting through flow-induced oscillations of a foil. *Physics of Fluids*, 21, 123602.

[15] Young, J., Ashraf, M., Lai, J., et al. (2013). Numerical simulation of fully passive flapping foil power generation. *AIAA Journal*, 51, 2727 – 2739.

[16] ANSYS (2011). *ANSYS FLUENT User's Manual*. Canonsburg, USA: ANSYS Inc.

[17] Wang, Z., Du, L., Zhao, J., et al. (2017). Structural response and energy extraction from a fully passive flapping foil. *Journal of Fluids and Structures*, 72, 96 – 113.

[18] OpenFOAM (2015). The openfoam website: http://www.openfoam.com/.

[19] Spalart, P. and Allmaras, S. (1992). A one-equation turbulence model for aerodynamic flows. Reno, USA: 30th Aerospace Sciences Meeting and Exhibit.

[20] Travin, A., Shur, M., Strelets, M., et al. (2000). Detached-eddy simulations past a circular cylinder. *Flow Turbulence and Combustion*, 63, 293 – 313.

[21] Newmark, N. (1959). A method of computation for structural dynamics. *Journal of the Engineering Mechanics Division*, 85(EM3), 67 – 94.

[22] Murua, J., Palacios, R., and Peiró, J. (2010). Camber effects in the dynamic aeroelasticity of compliant airfoils: bifurcation and chaos. *Journal of Fluids and Structures*, 26, 527 – 543.

[23] Gsell, S., Bourguet, R., and Braza, M. (2016). Two-degree-of-freedom vortex-induced vibrations of a circular cylinder at re = 3900. *Journal of Fluids and Structures*, 67, 156 – 172.

[24] Zhu, Q. (2011). Optimal frequency for flow energy harvesting of a flapping foil. *Journal of Fluid Mechanics*, 675, 495 – 517.

[25] Sarkar, S. and Bijl, H. (2008). Nonlinear aeroelastic behaviour of an oscillating airfoil during stall-inducd vibration. *Journal of Fluids and Structures*, 24, 757 – 777.

COPYRIGHT STATEMENT